

The Stabilized Explicit Variable-Load Solver with Machine Learning Acceleration for the Rapid Solution of Stiff Chemical Kinetics

K. Buchheit^{a,b}, O. Owoyele^{a,b}, T. Jordan^a, D.T. Van Essendelft^a

^a National Energy Technology Laboratory, Morgantown, WV 26505, USA

^b Oak Ridge Institute for Science and Education, Oak Ridge, TN 37831, USA

Abstract

Numerical solutions to differential equations are at the core of computational fluid dynamics calculations. As the size and complexity of the simulations grow, so does the need for computational power and time. Solving the equations in parallel can dramatically reduce the time to solution. While traditionally done on CPU, unlocking the massive number of computational cores on GPU is highly desirable. Many efforts have been made to implement stiff chemistry solvers on GPU's but haven't been highly successful because of the logical divergence in traditional stiff algorithms like CVODE or LSODE. This study will demonstrate a machine learned hybrid algorithm implemented in TensorFlow for stiff problems and the speed gains relative to the traditional LSODE solver used in the Multiphase Flow with Interphase eXchanges (MFiX) Computational Fluid Dynamics (CFD) code. The results will show a dramatic decrease in total simulation time while maintaining the same degree of accuracy.

1. Introduction

Computational Fluid Dynamics (CFD) provides an excellent means to simulate a real system and gain additional physical information with minimal cost. In a reacting system, the addition of the chemistry source terms to the existing mass, energy, and momentum equations can dramatically increase the simulation times. In the case of stiff sets of chemical reactions, the simulation time could be completely dominated by the solving of the Ordinary Differential Equations (ODEs) tied to the species rates. This study aims to improve time to solution of the chemical rate integration by implementing a novel Stabilized, Explicit, Variable-load (STEV) solver method on both CPU and GPU by merging TensorFlow with MFIX.

TensorFlow is a static graph machine learning framework developed by Google.^[1] It is now a flexible platform for a range of tasks that utilizes dataflow programming. The static graph methods in TensorFlow allows it to run an algorithm on multiple operating devices, such as CPUs, GPUs, or TPUs. This saves development time of the algorithm and allows for ease of deployment without needing to specify instructions for how the program should run on a given piece of hardware. This feature allows TensorFlow to be used as an exceptionally flexible and efficient math library to test deployment of algorithms across a wide variety of the latest hardware accelerators that is not strictly limited to machine learning applications.

Most ODE solvers used in the solution of stiff chemistry utilize some form of implicit finite difference scheme such as the backward differentiation formula due to their ability to remain stable while taking relatively large time steps when compared to explicit methods. Implicit methods require the solution of non-linear (often system of) equations at each time step. Multi-core CPUs can handle the various logic elements present in an implicit solver algorithm as each thread can act independently. However, the same implicit methods implemented on the GPU have often ended up being slower than the CPU due to warp divergence.^[2-5] This study aims to implement a novel STEV method that can maintain warp convergence which will utilize the full parallelism of a GPU and solve stiff sets of ODEs. Further, this study aims to accelerate the STEV method by hybridizing the solver with machine learning techniques.

2. The Stabilized, Explicit, Variable-load (STEV) Solver

It is well known that explicit integrators suffer from stability issues which drives the allowable time step to be small especially for stiff systems of equations. Thus, explicit methods have largely been abandoned in favor of implicit methods. That said, state of the art implicit methods require a significant level of logic within the algorithm to determine time step and order which results in poor performance on GPU's. The STEV solver incorporates several stabilization methods and allows each cell to advance on its own time step and cells are removed as they reach the desired integration time. In doing so, warp convergence is maintained which maximizes the efficiency on the GPUs.

In general, unstabilized explicit integrators will over step in concentration or time which will cause inaccurate integration, negative concentrations, and/or ringing. To extend the applicability of explicit methods into stiffer regions, targeted stabilization methods were developed which limit the negative effects. Much of the overstepping can be limited by smart choices for the integration time step (see section 2.1), the negative concentration issues can be further augmented by species stabilization (see section 2.2), and the ringing can be partially stabilized with DFT stabilization (see section 2.3)

2.1 Variable Time Step Stabilization

The first unique characteristic of the STEV solver is that each cell can evolve on its own time step. While the accuracy of explicit methods is largely dependent on the time step, there is no need for the entire field to evolve at the same time step, only that each cell integrates to the same end in time.

The time step stabilization works to limit both the maximum time step and the maximum species consumption as seen in Eqs. (1) to (5) and graphically represented in Figure 1.

$$r_i^* = \max(-r_i, 1.0 \times 10^{-30}) \quad \forall i \in (1 \dots n) \quad (1)$$

$$y_i^* = \begin{cases} 0.9y_i & \text{if } y_i \ll 1 \times 10^{-20} \\ 1.0 & \text{otherwise} \end{cases} \quad (2)$$

$$t^* = \min_i \left(\frac{\min(Y_{step}^{max}, y_i^*)}{r_i^*} \right) \quad (3)$$

$$\Delta t_{max} = t_f \cdot \delta^{max} \quad (4)$$

$$h = \min(t^*, \Delta t_{max}) \quad (5)$$

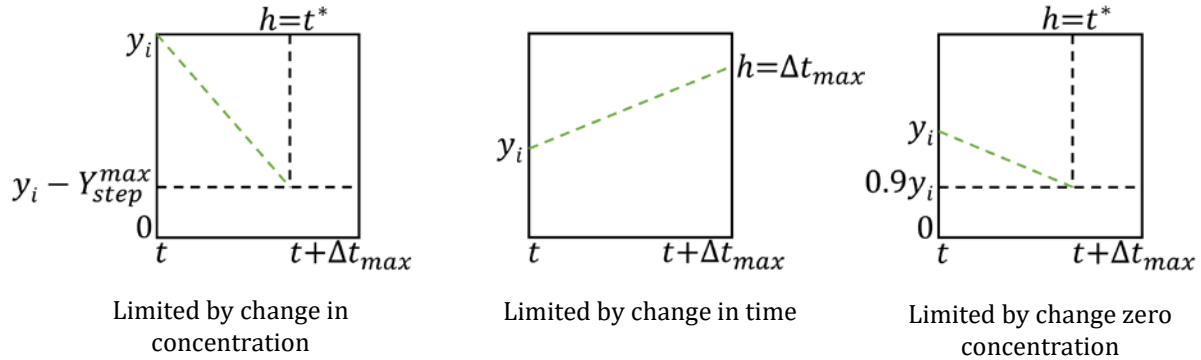


Figure 1: Graphical representation of time step stabilization

Here, h is the time step calculated for each cell, y_i is the species concentration in each cell, r_i is the species rate of change in each cell, Y_{step}^{max} is the maximum allowed species consumption at each step, t_f is the total integration time, δ^{max} is a fraction which limits the maximum allowed time step, and Δt_{max} is the maximum allowed time step.

The objective Eq (3) is to calculate allowable time step which will limit consumption to either a predefined maximum species consumption, Y_{step}^{max} , or ninety percent of the current species concentration. Species generation is not strictly controlled. However, by carefully controlling consumption and by the law of mass action, species generation is proportionally limited. Further, the species concentrations are appropriately controlled to be between zero and unity.

It is also worth noting that limiting the time step in this way effectively makes explicit methods usable for nearly infinitely stiff irreversible reactions if the time step can be represented within the numeric

precision chosen. Moreover, it helps to increase the integration accuracy by dynamically limiting the changes when the rates are high in magnitude.

The objective of Eq (4) is to prevent over stepping when dealing with something like delayed ignition. In such cases, the temperature limits the stiff chemistry and it is necessary to control the time step to obtain the correct ignition delay. Typically, if ignition delay is important t_f in the simulation is small and a fraction δ^{max} of between 0.001 and 0.01 is sufficient. Care should be taken in choosing this factor because it directly impacts the number of steps the solver must take to reach t_f (i.e. the amount of time it takes for the solver to complete the integration).

2.2 Small Species Stabilization

For species which can be consumed, a term was added to the chemical reaction rates which artificially slows reactions in the limit of small concentrations. That is, y_i is replaced with $\gamma(y_i)y_i$ in the rate equations where:

$$y_i^{**} = y_i\gamma(y_i) \quad (6)$$

$$\gamma(y_i) = \frac{y_i}{(\alpha + y_i)} \quad (7)$$

Here, y_i^{**} is the effective species concentration, α is a species limit factor such that when $y_i \gg \alpha$, $\gamma(y_i)$ is unity and when $y_i \ll \alpha$, $\gamma(y_i)$ is zero. Typical values for α are near 1×10^{-5} . This stabilization technique works in conjunction with Eq (3) to smooth the transition of a stiff reactions when reagents approach a near zero concentration and lowers the number of steps needed to integrate in these cases. Typically, extremely low species concentrations are not important. If they are, lowering α or not using this technique is advisable.

2.3 Discrete Fourier Transform (DFT) Stabilization

The techniques in sections 2.1 and 2.2 help stabilize irreversible reactions and reactions with species concentrations near zero. However, they typically will not help in cases of stiff reversible reactions where the equilibrium point is not near zero species concentrations. In detailed combustion mechanisms, these reactions are common.

To help stabilize these rate expressions, a methodology based on the DFT of the change in reaction progress for the reversible reactions was developed. In this method the change in reaction progress for each cell is calculated and stored in an array as in Eq (8).

$$r_{store}^i = r_{rev}h \quad (8)$$

Here, r_{store}^i is the i^{th} stored value of the change in reaction progress, r_{rev} is a reversible reaction rate, and h is the time step. Typically, only the thirteen most changes in reaction progress are kept for calculating the DFT. The magnitude of the DFT of r_{store}^i is taken at each integrator time step and a ringing factor is calculated

$$D_{rev} = |DFT(r_{store}^i)| \quad (9)$$

$$f_{ring} = \frac{D_{rev}^0}{\max(D_{rev}^j |_{n < j < N})} \quad (10)$$

Here, D_{rev} is the magnitude of the DFT for each cell, D_{rev}^j is the j^{th} frequency component of the DFT, n denotes the start of high frequency components, N is the highest frequency component, and f_{ring} is the ringing factor. If the low frequency term dominates f_{ring} , then it is near unity. As ringing occurs f_{ring} drops. Further, as equilibrium is attained D_{rev}^0 approaches zero. Thus, the ringing equilibrium condition is detectable and controllable through Eqs (11) to (14).

$$rOF_0 = 1.0 \quad (11)$$

$$rOF^* = \begin{cases} 1.0/r_{fac} & \text{if } f_{ring} < Tol_{ring} \text{ and } D_{rev}^0 < Tol_{freq} \\ r_{fac} & \text{otherwise} \end{cases} \quad (12)$$

$$rOF_{t+1} = \min(rOF^*, 1.0) * rOF_t \quad (13)$$

$$r_{rev}^{eff} = r_{rev} * rOF_t \quad (14)$$

Here, rOF denotes the rate oscillation factor and is limited to the range $0 < rOF \leq 1.0$. The subscript on rOF denotes the time step where 0 is the initial time step, t is the current time step, and $t+1$ is the next time step. Tol_{ring} is a ringing tolerance which sets the allowable level of ringing and Tol_{freq} is the low frequency tolerance which sets the threshold for equilibrium detection. Finally, r_{fac} is the factor which determines how quickly to damp the reversible rate and r_{rev}^{eff} is the effective rate used in the integration. rOF is initialized as 1.0 and will not decline unless the reversible rate is both ringing and at equilibrium. If the reversible rate meets these criteria, it will quickly be dampened so that equilibrium is maintained, and the integration can continue without such small time steps. If the conditions change, the rate is quickly brought back up to full speed.

This method of controlling ringing was tested with the BFER mechanism for methane and found to be able to integrate these equations with good performance. The BFER mechanism is a six species, two step mechanism which was reduced from GRIMECH and fairly accurate with equivalence ratios below about 1.3.^[4,5] The important thing to note is that both reaction steps are exceptionally stiff and the CO oxidation reaction is reversible.

That said, several detailed mechanisms like GRIMECH have many stiff, reversible, and competitive reactions. The performance of the STEV solver with DFT stabilization was degraded as the number of stiff, reversible, and competitive reactions increased and did not integrate GRIMECH well without using very small time steps. Performance improvements are still under development. However, the current version of the STEV solver is expected to perform well with almost all global combustion mechanisms and many analytically reduced mechanisms.

2.4 Variable Loading

Because each cell can evolve at its own time step, each cell will reach the final integration time at a different iteration. To deal with this additional complexity, a variable is initialized that contains the initial thermochemical state (species concentrations, temperature, and pressure). As cells reach the

final integration time, the end thermochemical state is copied to the variable and the cell is removed from further calculation. In this way, the solver only works on unfinished cells at all time steps and maintains a logical coherence that results in no thread divergence. The only thing that changes is the “load” which is the number of cells that are being iterated at any given step. The STEV solver has the characteristic that for the first $1/\delta^{max}$ iterations, every cell is active. After that number of iterations, cells can drop out leaving only cells with stiff conditions. For computational fluid dynamics, this characteristic is extremely valuable as truly stiff conditions exist for a small portion of the simulation where there is a mix of oxidants and fuels and high temperatures. In this way, the STEV solver works only as hard as conditions in the simulation demand and can operate with near ideal parallelization.

3. The Machine Learning Accelerated STEV (MLA-STEV) Solver

Stiff chemistry solvers fall into the class of Initial Value Problems (IVPs) while most other problems in CFD are Boundary Value Problems (BVPs). This distinction turned out to be quite important in efforts to hybridize the STEV solver with Machine Learning (ML). The problem with using ML to predict the integration of the thermodynamic state is that the accuracy of the predicted state (while good by ML standards) is not sufficient when the thermodynamic state is repeatedly fed into the ML model as is done while running CFD. Multiple studies have focused on training neural networks for thermochemical integration.^[6, 7] Significant accuracy gains were obtained relative to previous work with ML predictions of thermochemical states in this study. However, even with relative prediction errors reaching as low as 1×10^{-5} , the solution temperature in CFD slowly walked away from a physically meaningful value.

While it is true that evaluating the ML based predictions are exceptionally quick, the nature of the IVP does not allow for efficient correction of the ML prediction because any correction methodology involves either: 1) integration from the initial condition or 2) a large number ML predictions to form an time field as an initial guess to formulate the solution method as a nonlinear BVP. There is no point in correcting via 1) as it is just as much computational effort as integration by standard IVP solution methods. The computational efficiency of the ML predictions in 2) is diluted by the number of samples needed to establish the initial field and the computational effort of the nonlinear BVP solver. Further, is not possible to know how many samples are needed to maintain stability nonlinear BVP solver a priori.

Thus, ML acceleration was limited to indirect property calculations for thermodynamics as prediction errors were lower overall and errors had a lower impact on simulation results. The adiabatic temperature dependence in the system of ODEs requires the specie thermodynamic properties of enthalpy and heat capacity to be estimated. A common method of computational estimation involves the use of the NASA 7 polynomials which follow the forms in Eqs (15) and (16).

$$\frac{C_p}{R} = a_1 + a_2 T + a_3 T^2 + a_4 T^3 + a_5 T^4 \quad (15)$$

$$\frac{H}{RT} = a_1 + \frac{a_2 T}{2} + \frac{a_3 T^2}{3} + \frac{a_4 T^3}{4} + \frac{a_5 T^4}{5} + \frac{a_6}{T} \quad (16)$$

Where C_p is the constant pressure heat capacity, H is enthalpy, the ideal gas constant R , T is the species temperature, and a_i is the i coefficient in the series. The thermodynamic properties are also represented across a temperature range with at least one split temperature, $T_{low} < T_{split} < T_{high}$, with

a set of coefficients for each range. For calculation at run time, vectors of temperature need to be evaluated logically to determine where the temperature of each individual reacting cell falls into these ranges to use the correct coefficients. Enthalpy and heat capacity are smooth and continuous functions for each specie that is not undergoing a phase transition which makes it simple to estimate by a neural network. A single Artificial Neural Network (ANN) was trained to estimate the thermodynamic properties for all phases and all species simultaneously.

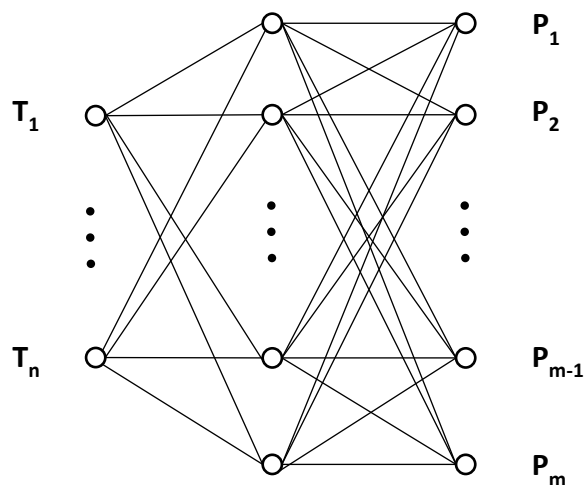


Figure 2 - Neural Network Structure

The inputs to the ANN are the temperatures for each phase and the outputs are the species properties of interest (specific heat or enthalpy for each species). Given the simplicity of the task, a single hidden layer was used with a sigmoid activation. The width of the hidden layer was set to the width of the number of output properties. The output layer used a linear activation. Figure 2 shows the simple structure for the ANN estimator. Training was performed by randomly sampling across the temperature range for the polynomials independently for each phase to generate species thermodynamic properties. The data was split into two groups for training and testing. Given the low number of free parameters in the model and ease of generating training data, the input domain was simply heavily over sampled to prevent over fitting. Optimization of the neural network was performed with a custom solver implementation of the Levenberg Marquardt Algorithm (LMA) in TensorFlow. The LMA is known to be much more efficient than gradient descent methods when the number of samples and variables is small as the Jacobian and Hessian need to be calculated.

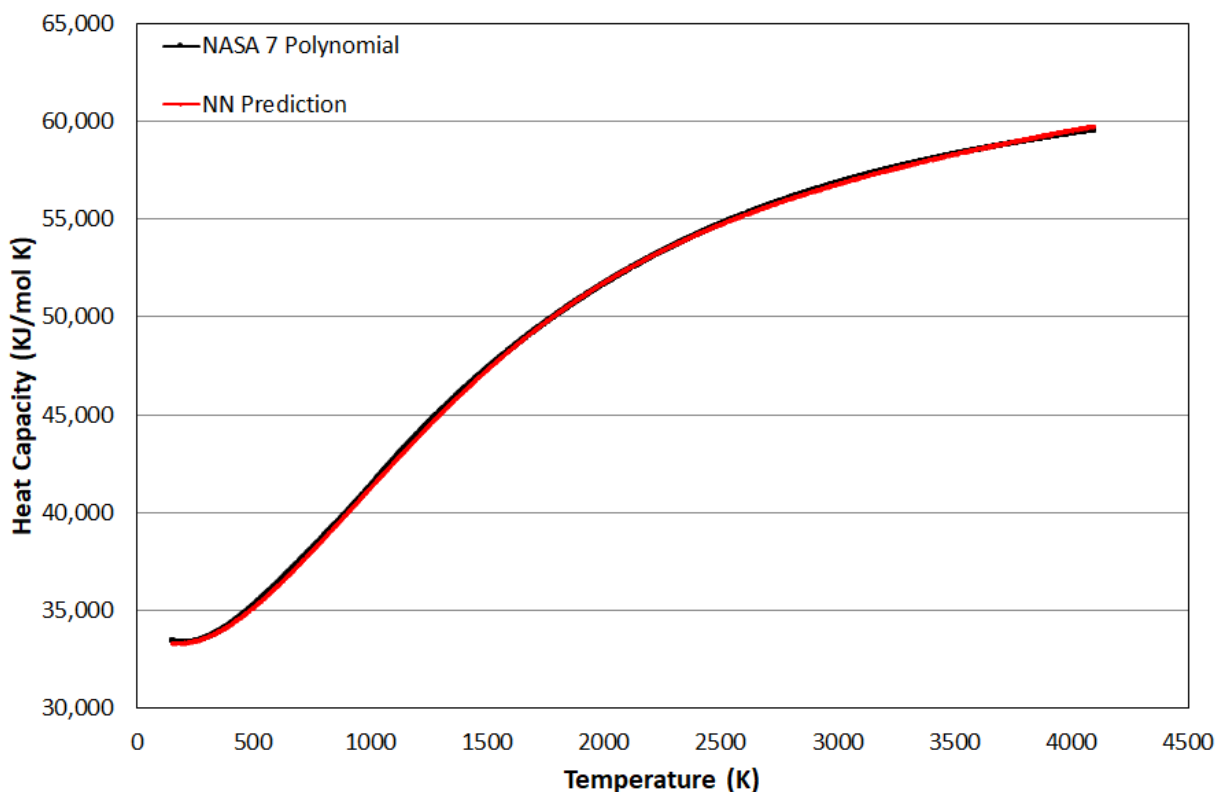


Figure 3 – Example ANN model estimation for the specific heat of water vapor

Figure 3 shows the ANN estimation and training data for the specific heat of water vapor. The ANN has a maximum of 0.436% difference from the polynomial calculation and an average difference of 0.138%.

Even though the thermodynamic properties are traditionally evaluated via simple polynomials, it was found that replacing them with an ANN estimation saved considerable calculation time. On average, evaluating the ANN was about 20% faster than calculating all the species properties via the polynomials. The thermodynamic calculations needed to calculate the rate of change of temperature are not an insignificant part of each iteration. The exact amount depends on the number of species relative to the number of reactions, but most global mechanisms are roughly equal. Experience has shown that the thermodynamic calculations account for roughly half of the computational effort for global mechanisms. Thus the 20% speed up obtained via ANN estimators translates to about a 10% reduction in time to solution. The speed gains could be even more substantial on a Volta architecture if the mixed precision tensor cores are used for the evaluation of the ANNs as they are known to accelerate ANN evaluations by as much as five times. When the sampling and training of the ANN is so quick and automated using the LMA with oversampling, this speed gain is simple and quick to obtain.

4. The Absolute Stability Analysis of the Forward Euler STEV Solver

Assuming that reactions are elementary, the rates of change of the thermochemical state are a function of the thermochemical state as in Eq (17).

$$\mathbf{X}' = \mathbf{f}(\mathbf{X}) \quad (17)$$

The Forward Euler finite difference method is the simplest and most straightforward explicit solution estimator for ODEs. It is derived simply from the first order linear approximation of a differential equation by Taylor Series expansion resulting in the following scheme:

$$\mathbf{X}_{i+1} = \mathbf{X}_i + hf(\mathbf{X}_i, t_i) \quad (18)$$

Where x represents the state variable at a point in time i , h is the step size between the current and the next point in time, and f is the right-hand side function evaluated at the current step.

The absolute stability criteria for the Forward Euler method requires that the eigenvalues of the coefficient matrix be bounded by the disk of radius 1 centered at -1 in the left half of the complex plane:

$$|1 + h\lambda| \leq 1 \quad (19)$$

Where λ is a representative eigenvalue. A first order approximation of the non-linear representative system of equations shown in Eq (17) by Taylor Expansion is:

$$\mathbf{X} := \mathbf{X}_0 + \Delta\mathbf{X} \quad (20)$$

For small enough step changes $\Delta\mathbf{X}$ in the state vector variable \mathbf{X} from an initial state \mathbf{X}_0 .

$$\mathbf{X}'_0 + \Delta\mathbf{X}' \approx \mathbf{f}(\mathbf{X}_0) + \left. \frac{\partial \mathbf{f}}{\partial \mathbf{X}} \right|_{\mathbf{X}_0} \Delta\mathbf{X} \quad (21)$$

Since $\mathbf{X}'_0 = \mathbf{f}(\mathbf{X}_0)$, a new linearized approximation emerges as:

$$\Delta\mathbf{X}' = \left. \frac{\partial \mathbf{f}}{\partial \mathbf{X}} \right|_{\mathbf{X}_0} \Delta\mathbf{X} \quad (22)$$

The local stability of Eq (22) is found by determining the eigenvalues of the Jacobian matrix evaluated at the initial condition as applied to Eq (19):

$$\mathbf{A} := \left. \frac{\partial \mathbf{f}}{\partial \mathbf{X}} \right|_{\mathbf{X}_0}, \rho(\mathbf{A}) = \sup\{|\lambda| : \lambda \in \sigma(\mathbf{A})\} \quad (23)$$

Where $\rho(\mathbf{A})$ is the spectral radius of the Jacobian matrix and λ is an eigenvalue of the spectrum, $\sigma(\mathbf{A})$. The eigenvalues for a real chemically reactive system are all negative and real,^[10] leading to the following stability criterion from Eq (19).

$$h \leq \frac{2}{\max_i \sum_{j=1}^n |a_{ij}|} = \frac{2}{\|\mathbf{A}\|_\infty} \leq \frac{2}{\rho(\mathbf{A})} = \frac{2}{\sup|\lambda|} \leq \frac{2}{|\lambda|} \quad \forall \lambda \in \sigma(\mathbf{A}) \quad (24)$$

Combining the stability criterion in Eq (24) with the time step determined from Eq (5) gives the absolute stability criterion for the STEV solver when the Euler Method is used.

$$h = \min \left(\min_i \left(\frac{\min(Y_{step}^{max}, y_i^*)}{r_i^*} \right), \Delta t_{max} \right) \leq \frac{2}{\max_i \sum_{j=1}^n |a_{ij}|} \quad (25)$$

5. CFD, TensorFlow, and the STEV Solver

In most modern CFD codes, integration of stiff chemistry is done by operator splitting. That is, the fluid is evolved separately from the chemistry so that the fluid equations can be solved on a larger time step and the chemistry can be solved on a substantially smaller step which saves computational effort for relatively minor inaccuracies. Without operator splitting, the entire system of coupled equations would have to be solved on at chemistry time step. As a demonstration, NETL's MFiX CFD code^[11] was coupled to TensorFlow using multilanguage compilation of a C interface that can pass memory directly to the python TensorFlow library which can execute the graph containing the STEV solver. In this way it functions as a drop-in replacement for traditional CFD Stiff Solvers in most any CFD code.

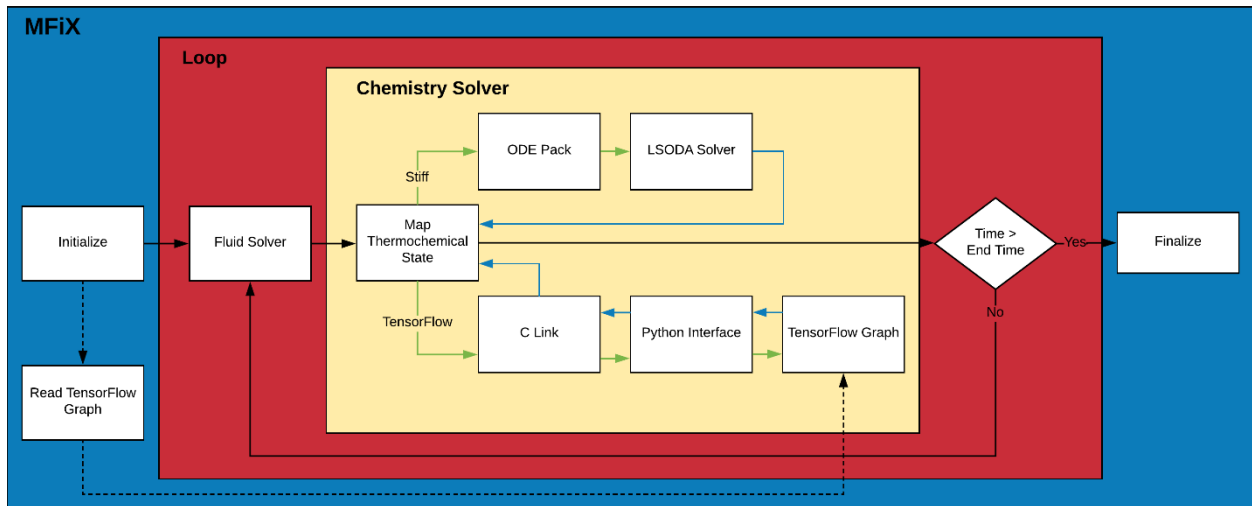


Figure 4: Integration of the STEV solver through TensorFlow in MFiX

To seamlessly integrate TensorFlow with MFiX, a switch statement was added enabling the user to choose to proceed through the original LSODA solver or bypass it through a simple variable declaration in the project file and perform the calculations within TensorFlow. An integration layer was developed that provides bi-directional communication between MFiX and TensorFlow which consists of a C link and a Python interface. The C link is called directly from the MFiX solver and provides the desired arguments in the form of memory pointers. Within the link, those pointers are then converted to python objects and passed along to the python interface. The interface then directly makes the necessary calls to the TensorFlow graph to perform the calculations. Those calculations are hardware agnostic and can be accelerated on any type of processing unit that TensorFlow supports. The results are then passed by reference back to the C link which in turn properly casts the memory and passes it back to the MFiX solver. MFiX then assigns those results to the thermochemical state. This implementation was chosen over the alternatives as the python API is the officially supported API for TensorFlow and it provides the most feature rich and simple interface.

6. Results and Discussion

Two test cases were completed with the integrated STEV solver in MFiX: A gas phase methane combustion case and a traditional gasifier. Tests were completed using the implicit LSODA based CPU solver in MFiX, and MLA-STEV solver in TensorFlow based on the CPU and GPU.

6.1 Gas Phase Methane Combustion

Initial testing of the TensorFlow implemented STEV Solver was performed in a gas phase only case using the BFER mechanism for methane oxidation.^[6]



$$r_{fwd} = k_{fwd} e^{-E_a/RT} C_{CH_4}^{0.5} C_{O_2}^{0.65} \quad (28)$$

$$r_{rev} = k_{rev} T^{0.7} e^{-E_a/RT} \left(C_{CO} C_{O_2}^{0.5} - \frac{C_{CO_2}}{K} \right) \quad (29)$$

$$K = \left(\frac{1 \text{ atm}}{RT} \right)^{\Delta N} e^{-\Delta G_{rxn}/RT} \quad (30)$$

Reaction	k	E_a (cal/mol)
<i>fwd</i>	4.9E+09	35500
<i>rev</i>	2.00E+08	12000

Reaction set based on the following units: cm, s, mol, cal

Where k is the rate constant, E_a is activation energy, R is the ideal gas constant, T is temperature, C is the concentration of the specie, K is the equilibrium constant, ΔN is the change in moles based on reaction stoichiometry, and ΔG_{rxn} is the change in Gibbs free energy due to the reaction.

The first set of timing experiments was conducted by running the solvers on the same set of random thermochemical states. Each chemistry solver was timed independently with an integration final time of 1 millisecond (a typical fluid time step) using increasing numbers of hypothetical cells. Since the thermochemical states are random but fixed, each solver operates on the same set of states at each fixed cell count. As the number of cells increases, the random states begin to cover the broad range of stiff and non-stiff combinations giving a more representative set of equations to solve. As can be seen from Figure 5, the time taken by the LSODA solver in MFiX exhibits an approximately linear and proportional behavior relative to the number of cells being solved. The MLA-STEV solvers run in TensorFlow exhibit a much different behavior with a nearly flat response out to a critical number of cells at which point memory saturation begins to affect the calculation speed. In as few as 200 cells, the CPU implementation becomes faster than the LSODA solver, and in as few as 1000, the GPU MLA-STEV solver becomes faster. In large scale simulations, the GPU MLA-STEV solver has the capability of being over

200 times faster than the LSODA solver. It is also worth noting that even when memory saturated, the GPU implementation continues to grow in relative speed increase because the memory access rate on the GPU is substantially higher than the CPU.

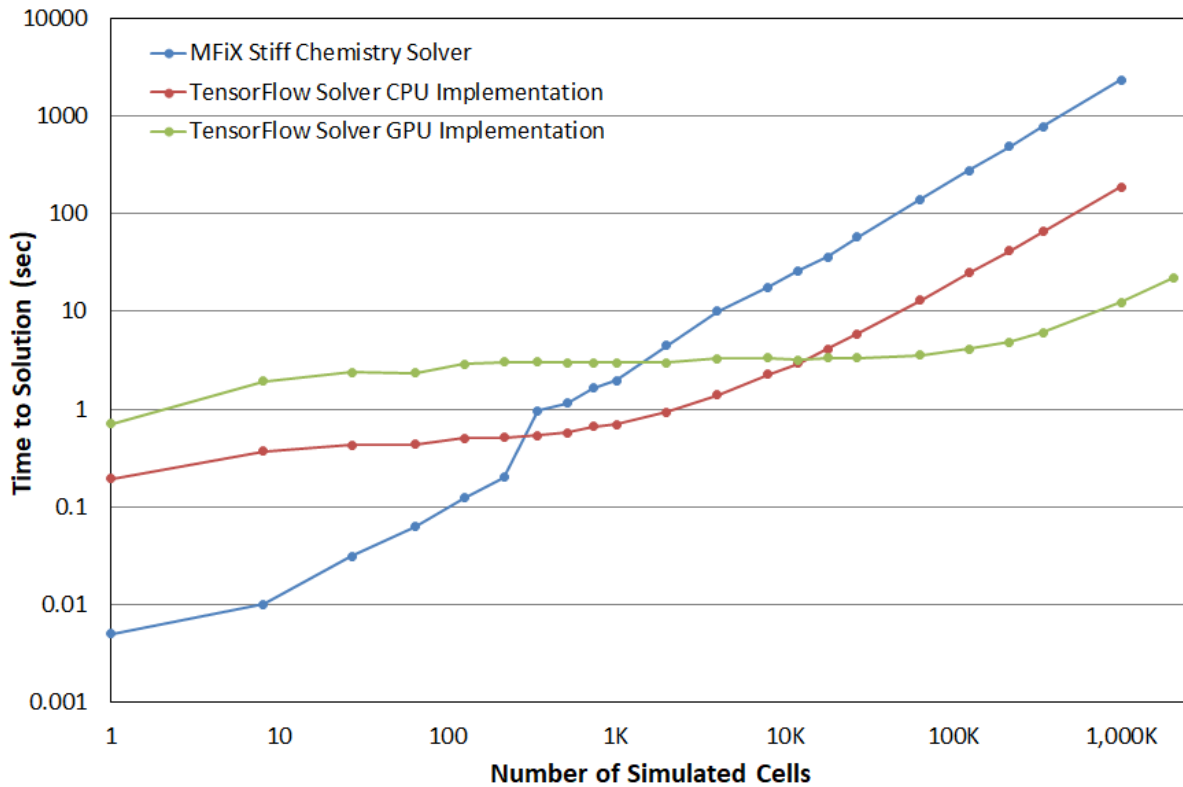


Figure 5 - Single phase chemistry with random cell compositions solver timing comparisons.

The second set of numerical experiments involved a fully developed diffuse flame CFD simulation run in MFiX. The flame was established using the default LSODA MFiX Stiff Chemistry Solver and run for several seconds to eliminate the effects of the initial condition. The restart checkpoint was used as the base for running the simulation an additional ten seconds of simulation time using each of the default MFiX Stiff Chemistry Solver, MLA-STEVE TensorFlow CPU solver, and MLA-STEVE TensorFlow GPU solver. The final second of each simulation was time averaged. The domain was sliced vertically in the middle of the flame and each cell was compared between the default LSODA MFiX Stiff Chemistry solver and the CPU/GPU MLA-STEVE Solver was calculated for each thermochemical property. The results from the CPU/GPU MLA-STEVE solvers were virtually identical. Figure 7-Figure 9 illustrates the minute differences between the LSODA solver and the GPU MLA-STEVE solver. The differences only occur along the reaction front.

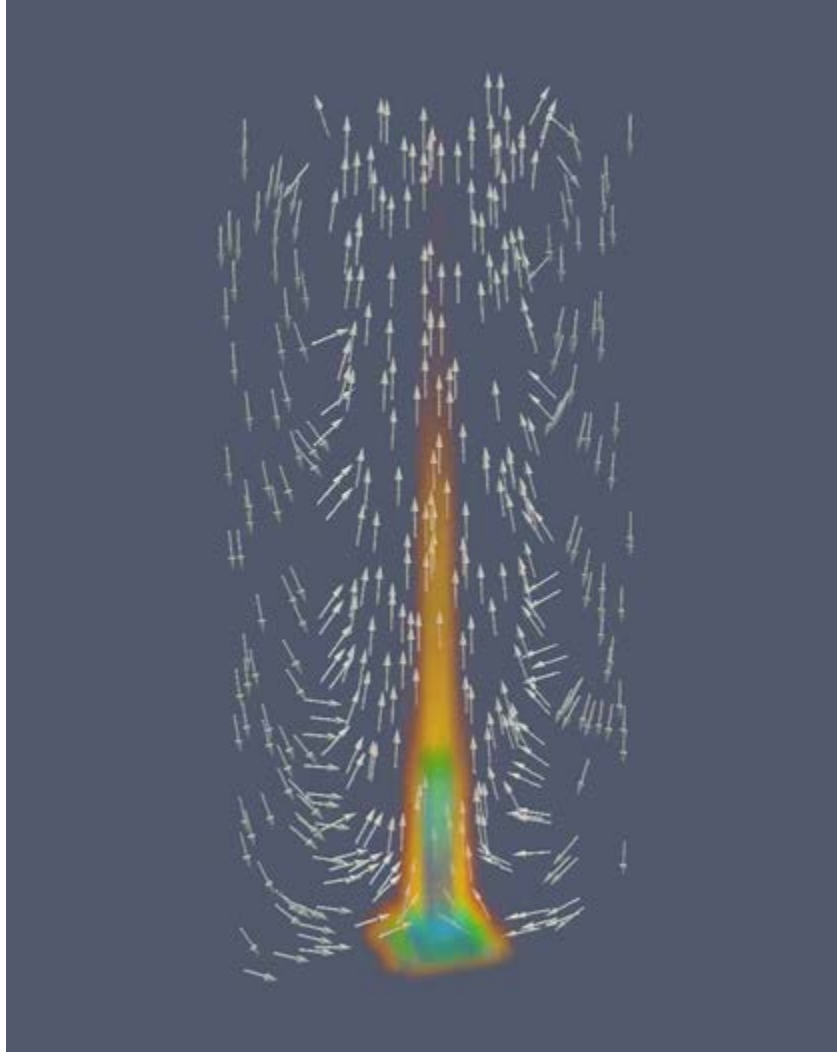


Figure 6 - Gas Phase Chemistry in Diffuse Flame CFD simulation. Colored by combustion species

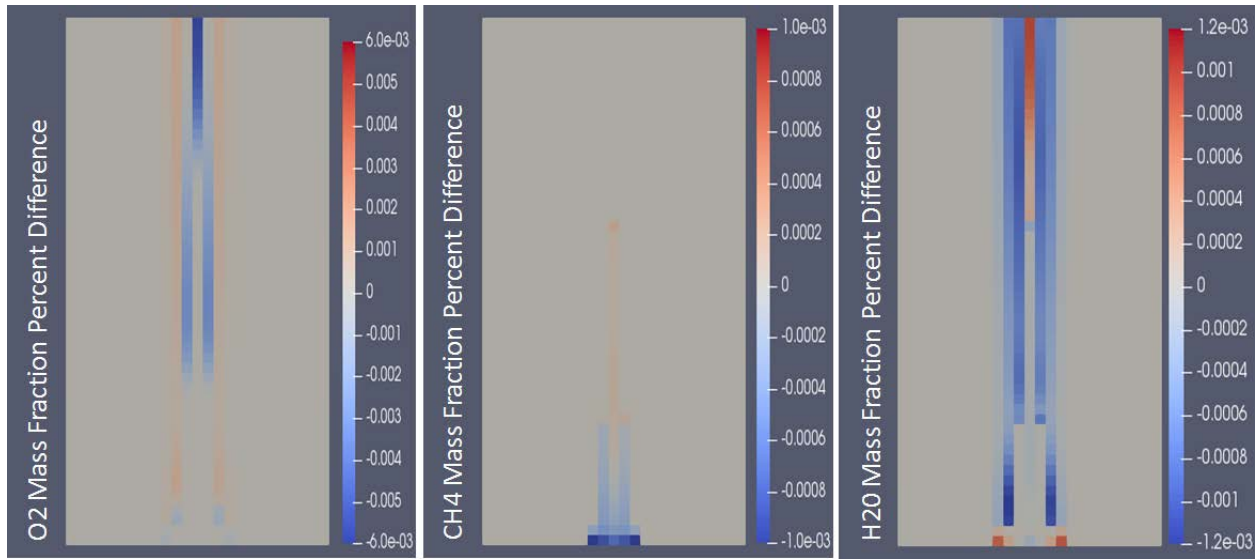


Figure 7 - Percentage difference between the LSODA Solver and the MLA-STEVE solver for O₂, CH₄, and H₂O mass fractions respectively

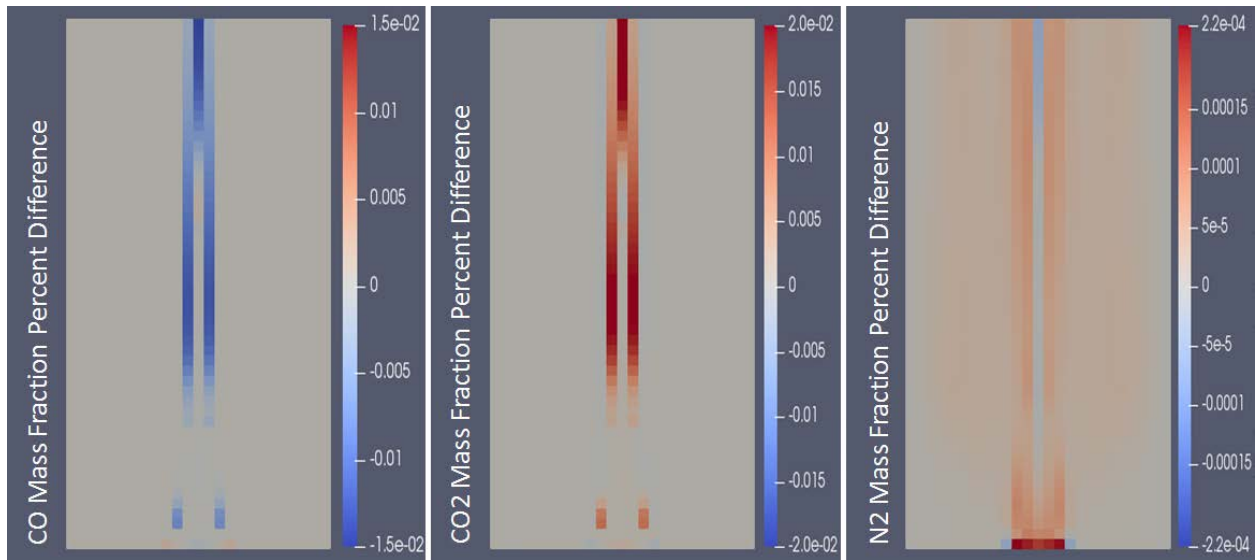


Figure 8 - Percentage difference between the LSODA Solver and the MLA-STEVE solver for CO, CO₂, and N₂ mass fractions respectively

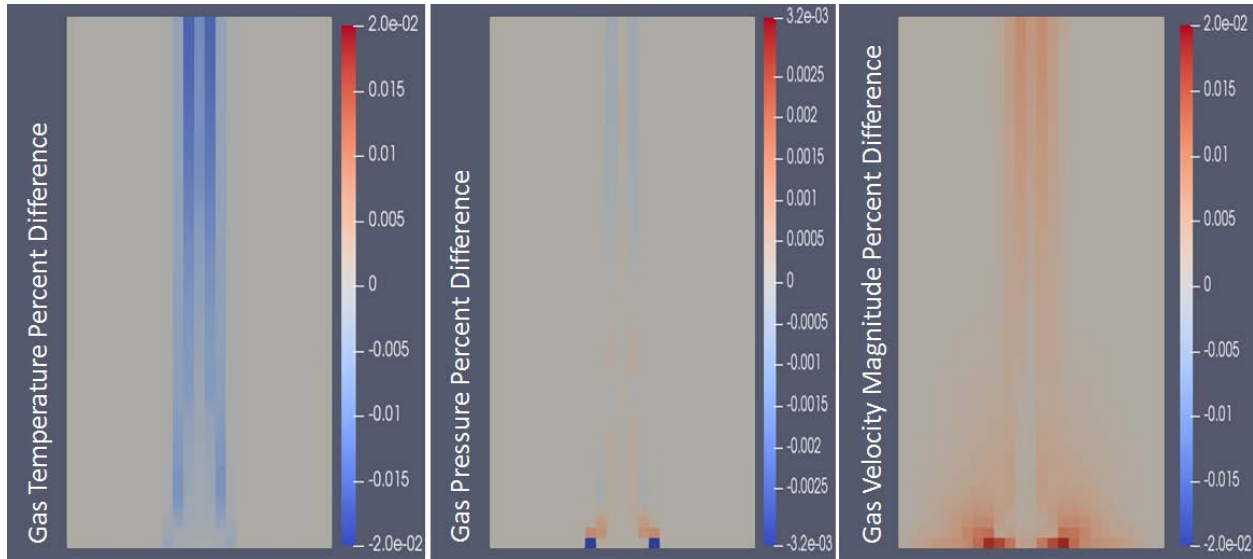


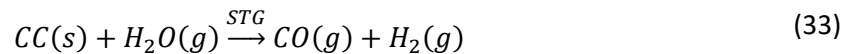
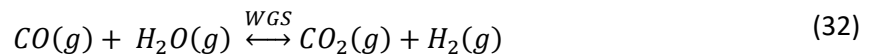
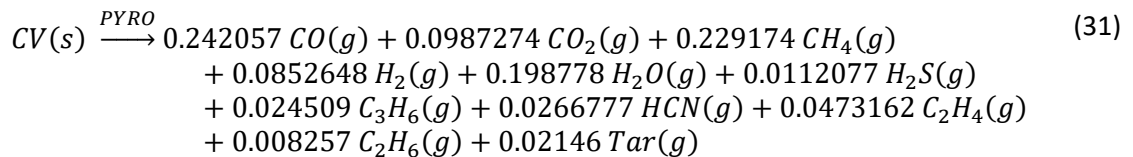
Figure 9- Percentage difference between the LSODA Solver and the MLA-STEVE solver for Temperature, Pressure, and Velocity Magnitude respectively

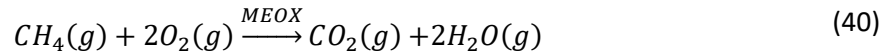
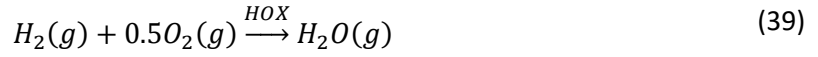
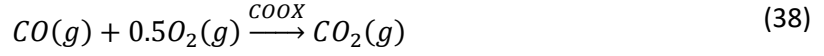
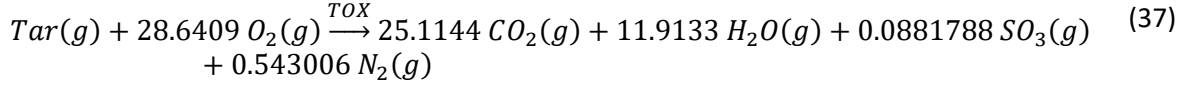
As can be seen, the simulations are virtually identical and match to within 0.006% in every case.

6.2 Multiphase Coal Gasification

Based on the success of the single-phase combustion case, the STEV solver was extended to handle multiphase reactions.

NETL's Carbonaceous Chemistry for Computational Modeling (C3M) was utilized to generate the chemical kinetics for gas-solid multiphase gasification.^[12]





$$r_{\text{PYRO}} = A_{\text{PYRO}} \varepsilon_s \rho_s X_{\text{CV}} \gamma(X_{\text{CV}}) e^{-E_{\text{aPYRO}}/T_s} \quad (42)$$

$$r_{\text{WGS}} = \varepsilon_g \varepsilon_s \rho_s (A_{\text{WGS}} P)^{(-F_{\text{P,WGS}} P + 0.5)} \left(K_{\text{F,WGS}} X_{\text{CO}} X_{\text{H}_2\text{O}} \gamma(X_{\text{CO}}) \gamma(X_{\text{H}_2\text{O}}) e^{-E_{\text{aWGS}}^{\text{F}}/T_g} - K_{\text{R,WGS}} X_{\text{CO}_2} X_{\text{H}_2} \gamma(X_{\text{CO}_2}) \gamma(X_{\text{H}_2}) e^{-E_{\text{aWGS}}^{\text{R}}/T_g} \right) \quad (43)$$

The gasification reactions (r_{STG} , r_{CG} , r_{MEG}) and char oxidation (r_{COX}) were derived from PC Coal Lab in C3M. They utilize an annealing factor, α_i , which is based on the reaction progress of conversion of fuel to ash. To keep the system stable in CFD, Eq (44) calculates the reaction progress factor, ϑ . The min and max statements help keep the reaction progress variable between zero and unity if the mass fractions are zero or negative. Eqs (47) to (50) use the annealing factor found in Eqs (44) and (46). In these equations, the i in Eq (46) is relative to gasification denoted by "G" or char combustion denoted by "C" Table 1.

$$\vartheta = \max\left(0, \min\left(1, \beta_c \frac{X_{\text{CC}}}{X_{\text{CA}}}\right)\right) \quad (44)$$

$$\varphi = 1 - \vartheta \quad (45)$$

$$\alpha_i = \varphi^5 + \theta_4^i \varphi^4 + \theta_3^i \varphi^3 + \theta_2^i \varphi^2 + \theta_1^i \varphi + \theta_0^i \quad (46)$$

$$r_{\text{STG}} = A_{\text{STG}} \alpha_G \varepsilon_s \rho_s X_{\text{CC}} \gamma(X_{\text{CC}}) \frac{\left(\frac{\text{MW}_g P_g X_{\text{H}_2\text{O}}}{18.01530}\right)^{0.98}}{1 + F_{\text{P,STG}} \left(\frac{\text{MW}_g P_g X_{\text{H}_2}}{2.01588}\right)} e^{-E_{\text{aSTG}}/T_s} \quad (47)$$

$$r_{CG} = A_{CG} \alpha_G \varepsilon_s \rho_s X_{CC} \gamma(X_{CC}) \frac{\left(\frac{MW_g P_g X_{CO_2}}{44.00980}\right)^{0.56}}{1 + F_{P,CG} \left(\frac{MW_g P_g X_{CO}}{28.01040}\right)} e^{-Ea_{CG}/T_s} \quad (48)$$

$$r_{MEG} = A_{MEG} \alpha_G \varepsilon_s \rho_s X_{CC} \gamma(X_{CC}) \left(\frac{MW_g P_g X_{H_2}}{2.01588}\right) e^{-Ea_{MEG}/T_s} \quad (49)$$

$$r_{COX} = \alpha_C A_{COX} \gamma(X_{O_2}) \gamma(X_{CC}) e^{-Ea_{COX}/T_{film}} \left(\frac{MW_g P_g X_{O_2}}{31.9988}\right)^{0.73} \varepsilon_s / d_p \quad (50)$$

$$T_{film} = 0.5T_g + 0.5T_s \quad (51)$$

$$r_{TOX} = A_{TOX} e^{-Ea_{TOX}/T_g} \varepsilon_g \rho_g^{1.75} X_{O_2}^{1.5} X_{Tar}^{0.25} \gamma(X_{O_2}) \gamma(X_{Tar}) \quad (52)$$

$$r_{COOX} = A_{COOX} e^{-Ea_{COOX}/T_g} \varepsilon_g \rho_g^{1.75} X_{O_2}^{0.25} X_{CO} X_{H_2O}^{0.5} \gamma(X_{O_2}) \gamma(X_{CO}) \quad (53)$$

$$r_{HOX} = A_{HOX} e^{-Ea_{HOX}/T_g} \varepsilon_g \rho_g^2 X_{O_2} X_{H_2} \gamma(X_{O_2}) \gamma(X_{H_2}) \quad (54)$$

$$r_{MEOX} = A_{MEOX} e^{-Ea_{MEOX}/T_g} \varepsilon_g \rho_g^{1.5} X_{O_2}^{1.3} X_{CH_4}^{0.2} \gamma(X_{O_2}) \gamma(X_{CH_4}) \quad (55)$$

$$r_{MR} = A_{MR} \gamma(X_{CM}) \varepsilon_s / d_p \quad (56)$$

Here, X is the mass fraction and the subscript denote that species formula. The species formula is symbolic of the most common compounds represented by those formulas. For example, O_2 is molecular oxygen and CH_4 is methane. However, CV is the coal volatile matter, CC is the coal fixed carbon, CM is the coal moisture, CA is the coal ash, and Tar is the tar produced by pyrolysis as a complex mixture of hydrocarbons. A is the pre-exponential factor and Ea is the activation energy. The subscript denotes the reaction they are a part of. There are also several phase properties denoted by a subscript g for gas or subscript s for solid. T is the phase temperature, ε represents the phase volume fraction, ρ is the phase density, MW is the mixture molecular weight, and P is the pressure. d_p is particle diameter and γ is the rate limit function defined in Eq (7). The constants for the model are defined in Table 1.

Table 1: Gasification Model Constants

Variable	Value
A_{PYRO}	$5.39808917197452 \times 10^{-1}$
Ea_{PYRO}	$2.02305749338465 \times 10^3$
A_{WGS}	$9.86923266716013 \times 10^{-6}$
$F_{P,WGS}$	$3.94769306686405 \times 10^{-8}$
$K_{F,WGS}$	$2.87480073925354 \times 10^0$
Ea_{WGS}^F	$8.42570940582151 \times 10^3$
$K_{R,WGS}$	$1.08482987533646 \times 10^2$
Ea_{WGS}^R	$1.23814194058215 \times 10^4$
θ_4^G	$-1.74119074065241 \times 10^0$
θ_3^G	$6.75755882493237 \times 10^{-1}$
θ_2^G	$2.42994500814316 \times 10^{-1}$
θ_1^G	$1.80861879808380 \times 10^{-1}$
θ_0^G	$-1.37554327457087 \times 10^{-1}$
θ_4^C	$-1.71305029851856 \times 10^0$
θ_3^C	$1.02332704517333 \times 10^0$
θ_2^C	$-2.12046897502992 \times 10^{-1}$
θ_1^C	$-4.34614630452274 \times 10^{-3}$
θ_0^C	$1.00829969505805 \times 10^{-2}$
A_{STG}	$3.64422300238124 \times 10^{-5}$
$F_{P,STG}$	$2.58573895879595 \times 10^{-7}$
Ea_{STG}	$4.27760404137599 \times 10^3$
A_{CG}	$1.21674169495915 \times 10^1$
$F_{P,CG}$	$2.57586972612879 \times 10^{-6}$
Ea_{CG}	$1.76136636997835 \times 10^4$
A_{MEG}	$1.66401967700346 \times 10^{-8}$
Ea_{MEG}	$9.15910512388742 \times 10^3$
β_c	$4.7741935483871 \times 10^{-1}$
A_{COX}	$2.16444452624815 \times 10^1$
Ea_{COX}	$1.43928313687756 \times 10^4$
A_{TOX}	$2.59900518618807 \times 10^6$
Ea_{TOX}	$1.50981378963261 \times 10^4$
A_{COOX}	$7.91515800843217 \times 10^9$
Ea_{COOX}	$2.01288244766506 \times 10^4$
A_{HOX}	$1.67426958313306 \times 10^{11}$
Ea_{HOX}	$1.50966183574879 \times 10^4$
A_{MEOX}	$1.34383699737932 \times 10^9$
Ea_{MEOX}	$2.43558776167472 \times 10^4$
A_{MR}	$1.0061447769396 \times 10^{-1}$

Like the single-phase solver numerical experiments, the multiphase chemistry was tested with a set of randomized thermochemical states used in each implementation. As in the single-phase case, the time to solution for the LSODA MFiX Stiff Chemistry solver increased linearly and proportionally to the number of cells being solved and there was also a similar trend for the STEV solvers in TensorFlow. Again, the CPU and GPU STEV solvers became faster than the LSODA solvers at roughly 100 and 1000 cells respectively. From Figure 10 the crossover point in solution time for the number of cells the CPU and GPU implementation of the STEV solver has extended to a much higher cell count versus the single phase example. This is likely due in part to the increased communication overhead needed to transfer a much larger thermochemical state on and off the GPU. For the single-phase case, only 8 thermochemical variables per cell needed to be transferred. For the multiphase case, there were 22 variables per cell. Even though there were lesser speed gains for the GPU STEV solver relative to the CPU STEV solver, the gains over the LSODA solver were substantial.

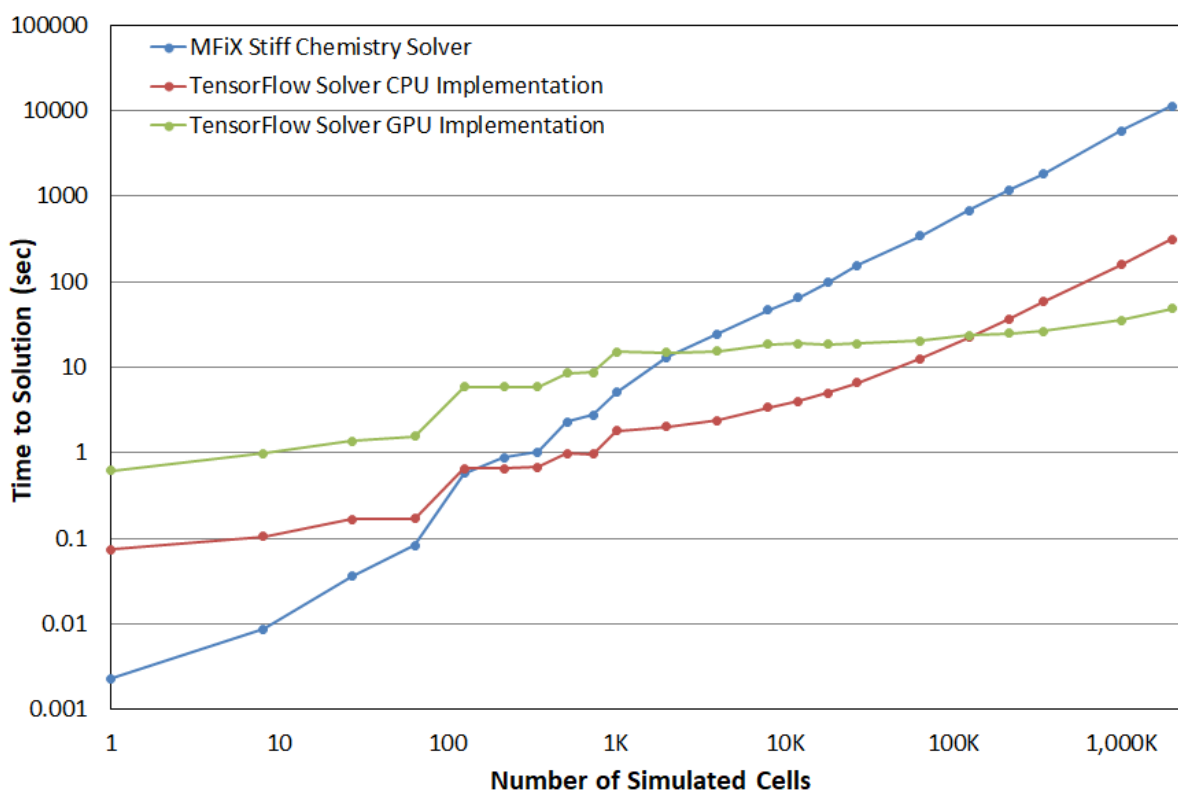


Figure 10 - Multiphase chemistry with random cell compositions solver timing comparisons.

To further understand the speed gains of the STEV solvers in the context of real world use, a second set of simulations was completed in which the number of cells of a gasifier were varied using the same setup from past analytical work at NETL with the Power Systems Development Facility transport gasifier.^[13] A range of grid resolutions resulting in various numbers of simulated cells was run. From Figure 11 and Figure 12 the time to solution for either the CPU or GPU STEV solver implementation of the TensorFlow solver were comparable and saved a significant amount of total simulation time as the cell count rose. The massive parallelization achieved through the STEV solver implementations greatly outpaced the increased time for setting up the graph used to solve the chemistry over the traditional

LSODA MFiX Stiff Chemistry Solver while maintaining comparable thermochemical states between the simulations.

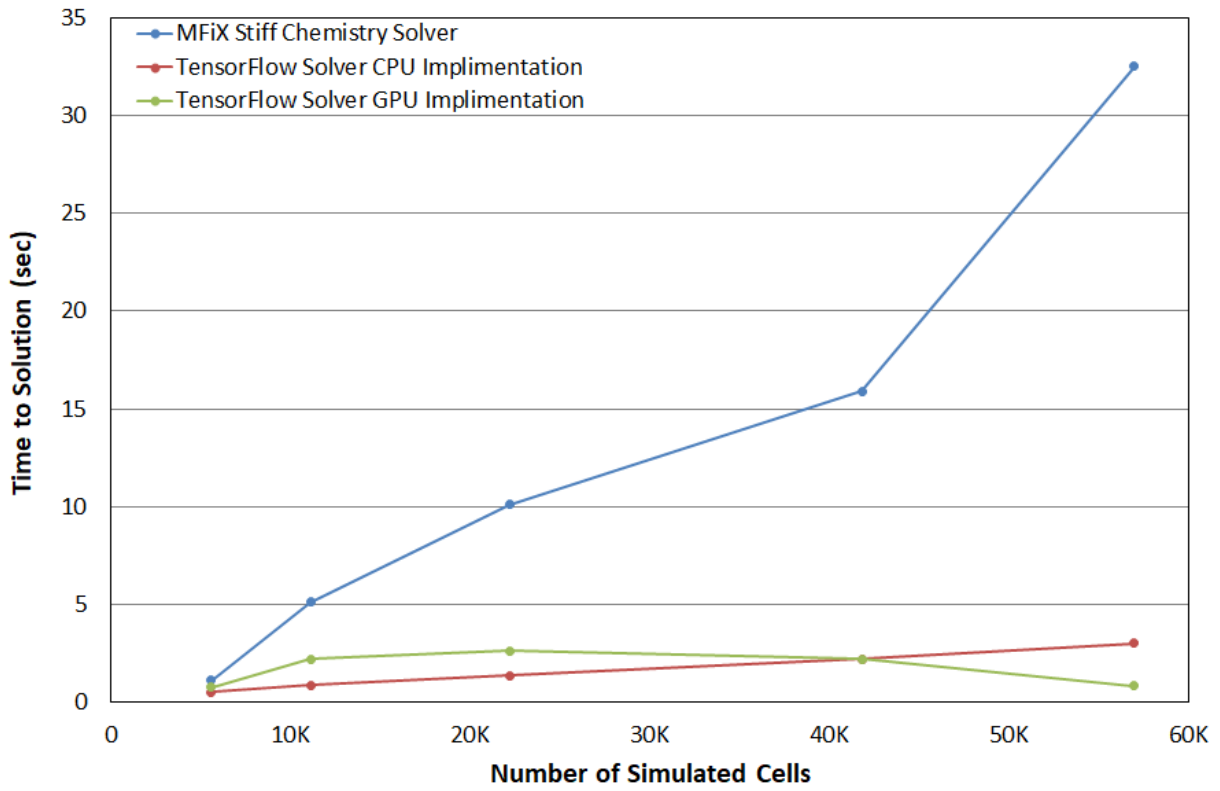


Figure 11: Average Stiff Solver solution time per fluid time step for multiphase gasification as a function of number of cells

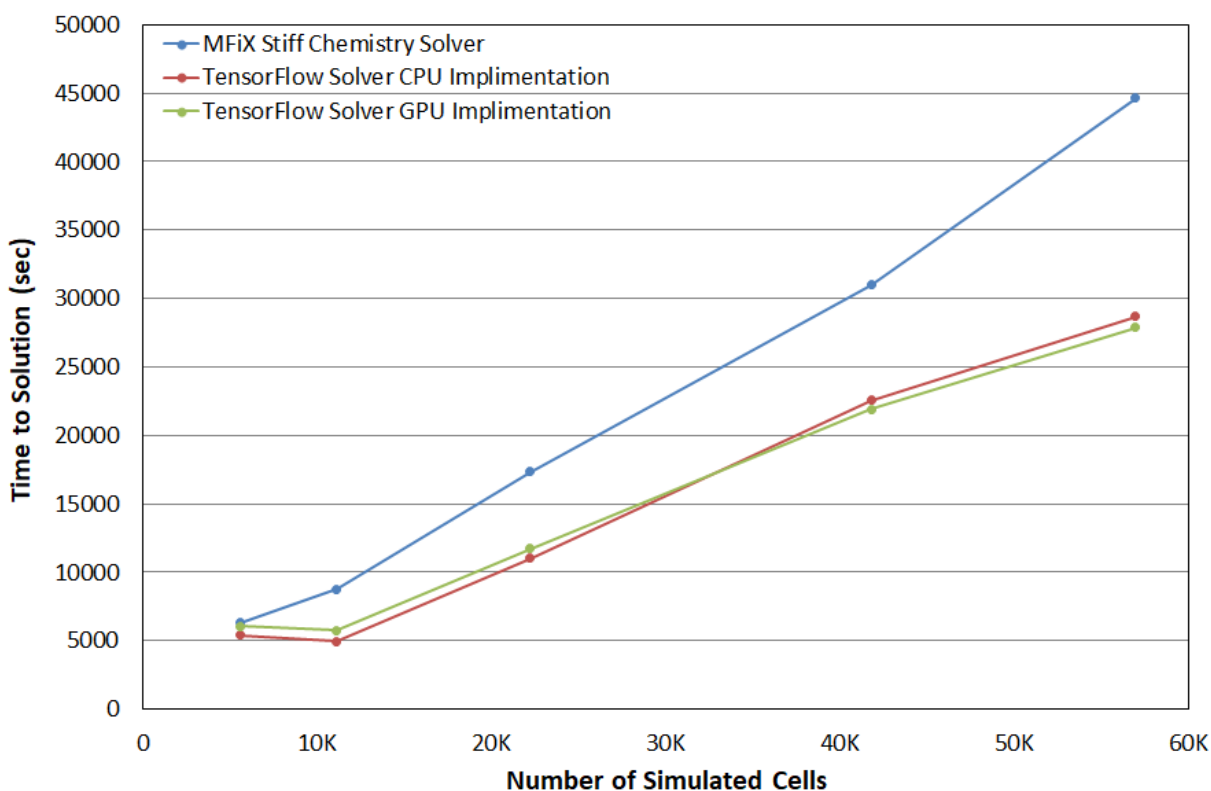


Figure 12: Total time to solution for transport gasifier simulations of varying resolutions for simulations of XX fluid seconds

7. Conclusions

The STEV solver was able to quickly and accurately predict the thermochemical state and dramatically reduce total simulation time through massive parallelization. The STEV solver was shown to be able to solve very stiff chemical equations much faster than the state-of-the-art implicit methods if there were few stiff, reversible, and competitive reactions present. The MLA-STEV solver was shown to be approximately 10% faster than the STEV solver. The GPU version of the STEV solver was found to be as much as 200 times faster than the LSODA CPU implementation. The CPU STEV solver tends to be faster than the GPU STEV solver when the cell count is lower and when mechanism size is large. However, for industrially relevant simulation sizes of multiple millions of cells, the GPU is likely to always be preferable.

8. Future Work

Because of the ease of defining device work using TensorFlow, the STEV solver could be further accelerated by exploring methods to divide the workload across multiple devices. It should be possible to avoid memory saturation for the same number of cells through this methodology which could greatly increase the speed for large simulation.

The parameters used in controlling the size of the time step can be optimized to result in a higher allowable time step while remaining stable and respecting potential issues with delayed ignition seen due to overstepping and under stepping from the Euler Method.

Different methods for controlling reaction rates near equilibrium could be explored to improve performance when many stiff, reversible, and competitive reactions are present. Perhaps ML methodologies could be employed to improve detection and response.

9. Acknowledgements

This research was performed under an appointment to the National Energy Technology Laboratory, administered by the Oak Ridge Institute for Science and Education under contract number DE-SC0014664 between the U.S. Department of Energy and Oak Ridge Associated Universities.

10. Disclaimer

This report was prepared as an account of work sponsored by an agency of the United States Government. Neither the United States Government nor any agency thereof, nor any of their employees, makes any warranty, express or implied, or assumes any legal liability or responsibility for the accuracy, completeness, or usefulness of any information, apparatus, product, or process disclosed, or represents that its use would not infringe privately owned rights. Reference therein to any specific commercial product, process, or service by trade name, trademark, manufacturer, or otherwise does not necessarily constitute or imply its endorsement, recommendation, or favoring by the United States Government or any agency thereof. The views and opinions of authors expressed therein do not necessarily state or reflect those of the United States Government or any agency thereof.

11. References

1. Abadi, M., P. Barham, J. Chen, Z. Chen, A. Davis, J. Dean, M. Devin, S. Ghemawat, G. Irving, and M. Isard. *Tensorflow: A system for large-scale machine learning*. in *12th {USENIX} Symposium on Operating Systems Design and Implementation ({OSDI} 16)*. 2016.
2. Brock, B., A. Belt, J.J. Billings, and M. Guidry, *Explicit integration with GPU acceleration for large kinetic networks*. *Journal of Computational Physics*, 2015. **302**: p. 591-602.
3. Curtis, N.J., K.E. Niemeyer, and C.-J. Sung, *An investigation of GPU-based stiff chemical kinetics integration methods*. *Combustion and Flame*, 2017. **179**: p. 312-324.
4. Sewerin, F. and S. Rigopoulos, *A methodology for the integration of stiff chemical kinetics on GPUs*. *Combustion and Flame*, 2015. **162**(4): p. 1375-1394.
5. Stone, C.P., A.T. Alferman, and K.E. Niemeyer, *Accelerating finite-rate chemical kinetics with coprocessors: Comparing vectorization methods on GPUs, MICs, and CPUs*. *Computer Physics Communications*, 2018. **226**: p. 18-29.
6. Franzelli, B., E. Riber, L.Y.M. Gicquel, and T. Poinot, *Large Eddy Simulation of combustion instabilities in a lean partially premixed swirled flame*. *Combustion and Flame*, 2012. **159**(2): p. 621-637.
7. Smith, G.P., D.M. Golden, M. Freklach, N.W. Moriarty, B. Eiteneer, M. Goldenberg, C.T. Bowman, R.K. Hanson, S. Song, W.C. Gardiner, V.V. Lissianski, and Z. Qin. *GRI-Mech 3.0*. [cited 2019; Available from: http://www.me.berkeley.edu/gri_mech/.
8. Blasco, J.A., N. Fueyo, J.C. Larroya, C. Dopazo, and Y.J. Chen, *A single-step time-integrator of a methane-air chemical system using artificial neural networks*. *Computers & Chemical Engineering*, 1999. **23**(9): p. 1127-1133.

9. Kelp, M., C. Tessum, and J. D. Marshall. *Orders-of-magnitude speedup in atmospheric chemistry modeling through neural network-based emulation*. 2018; Available from: <https://arxiv.org/abs/1808.03874>.
10. Summers, D. and J.M.W. Scott, *Systems of first-order chemical reactions*. Mathematical and Computer Modelling, 1988. **10**(12): p. 901-909.
11. Syamlal, M., W. Rogers, and T.J. OBrien, *MFIX documentation theory guide*. 1993, USDOE Morgantown Energy Technology Center, WV (United States).
12. Van Essendelft, D.T., T. Li, P. Nicoletti, and T. Jordan, *Advanced Chemistry Surrogate Model Development within C3M for CFD Modeling, Part 1: Methodology Development for Coal Pyrolysis*. Industrial & Engineering Chemistry Research, 2014. **53**(18): p. 7780-7796.
13. Li, T., W.A. Rogers, M. Syamlal, J.-F. Dietiker, J. Musser, M. Shahnam, and S. Rabha, *The NETL MFIX Suite of multiphase flow models: A brief review and recent applications of MFIX-TFM to fossil energy Technologies*. Chemical Engineering Science, 2017. **169**: p. 259-272.